

Postdeposition Ligand Exchange Allows Tuning the Transport Properties of Large-Scale CuInSe₂ Quantum Dot Solids

Friederike E. S. Gorris, Michael Deffner, Shekhar Priyadarshi, Christian Klinke, Horst Weller,* and Holger Lange*

Colloidal quantum dots assembled into quantum dot solids usually suffer from poor conductivity. The most common charge transport mechanism through the solid is hopping transport where the hopping probability depends on the barrier type (stabilizing/connecting ligand molecule) and the interparticle distance. It is demonstrated that the electronic structure of the ligand molecule strongly alters the transport behavior through CuInSe₂ quantum dot solids. Transport measurements and optical-pump terahertz-probe experiments after a ligand exchange to fully conjugated molecules show an increase of the conductivity by orders of magnitude, as well as a change of the hopping transport mechanism. This change is not due to a reduced interparticle distance, but the electronic structure: the obtained frequency-dependent complex conductivities point toward an efficient hole transport enabled by an alignment of the quantum dot valence bands and ligand states.

solids in applications such as light emitting devices^[4] and solar cells.^[5,6] A common problem of QD solids is charge transport. The large native ligands stabilizing the QDs reduce the electronic interparticle interactions, resulting in a low conductivity. Depending on the coupling between the QDs, the charge carrier transport mechanism can vary from a hopping-type to band-like transport.^[7] Band-like transport requires delocalized electronic wave functions. In larger QD solids, this is almost impossible to realize due to disorder and variations in QD size and shape, as well as insufficient coupling between the QDs.^[8] Reported QD solids with band-like transport feature interparticle distances reduced to a few Ångströms.^[9]

1. Introduction

Colloidal semiconductor nanocrystals, quantum dots (QDs), feature a size-dependent direct bandgap.^[1] The additional possibility to functionalize the QD's surface with different molecular ligands enables a broad range of applications.^[2] QDs can be assembled as QD solids where the ensemble (bulk) properties can be tailored by the choice of the constituting QDs and further modified by connecting ligands.^[3] This allows utilizing QD

But even QD solids with hopping as dominant carrier transport mechanism can be tuned to achieve high conductivities. The probability for the hopping (tunneling) process strongly depends on the local environment of the QDs, which determines the overlap of the electronic wave functions, and on the distance between the QDs.^[7,10] In general, hopping occurs to a site with the combination of shortest distance and lowest activation energy, described by the hopping probability $P \propto \exp(-2d/a - \Delta E/k_B T)$, where d is the hopping distance, a the

Dr. F. E. S. Gorris, M. Deffner, Dr. S. Priyadarshi, Prof. C. Klinke, Prof. H. Weller, Prof. H. Lange
Institute for Physical Chemistry
University of Hamburg
Martin-Luther-King Platz 6, 20146 Hamburg, Germany
E-mail: weller@chemie.uni-hamburg.de;
holger.lange@chemie.uni-hamburg.de

M. Deffner
Institute for Anorganic and Applied Chemistry
University of Hamburg
Martin-Luther-King Platz 6, 20146 Hamburg, Germany

 The ORCID identification number(s) for the author(s) of this article can be found under <https://doi.org/10.1002/adom.201901058>.

© 2019 The Authors. Published by WILEY-VCH Verlag GmbH & Co. KGaA, Weinheim. This is an open access article under the terms of the Creative Commons Attribution-NonCommercial License, which permits use, distribution and reproduction in any medium, provided the original work is properly cited and is not used for commercial purposes.

DOI: 10.1002/adom.201901058

M. Deffner, Prof. H. Weller, Prof. H. Lange
The Hamburg Centre for Ultrafast Imaging
22761 Hamburg, Germany

Prof. C. Klinke
Department of Chemistry
Swansea University
Swansea SA2 8PP, UK

Prof. C. Klinke
Institute of Physics
University of Rostock
Albert-Einstein-Straße 23, 18059 Rostock, Germany

Prof. H. Weller
Fraunhofer Center for Applied Nanotechnology CAN
Grindelallee 117, 20146 Hamburg, Germany

localization length, and ΔE is the activation energy, which depends on the electronic environment.^[11] An obvious approach to enhance the hopping transport is the reduction of the interparticle distance by utilizing short connecting ligands.^[10,12–14] Another, presently less elaborated approach is the tuning of the activation energy, mainly the electronic states between the QD's conduction and valence band states (CB and VB).^[15] Then hopping transport can be governed by the available density of states or Coulomb interactions.^[11,16] Consequently, ligands with molecular orbitals that mix with the QD band-edge states can improve the hopping transport.^[17] In principle, matching frontier orbitals of the barrier relative to the QD CB or VB could enable selective electron or hole transport.^[18,19] Up to today, systematic studies exploring the hopping tunability by the ligand's electronic structure are missing. For our exemplary study, we employ CuInSe₂ (CIS) QDs as QD material. CIS QDs are of particular interest as near-infrared absorption can be achieved and the material is less toxic than, for example, cadmium- or lead-based QDs.^[20] CIS QDs can be synthesized in solution and dispersed in various nonpolar solvents, enabling the deposition as thick films onto different substrates.^[21] An effective expansion of electron and hole wave functions into the ligand does not only depend on the prebinding energetic levels of QD CB or VB states with lowest unoccupied molecular orbital (LUMO) or highest occupied molecular orbital (HOMO) states, but also on the ligand's structural parameters such as the extent of their π -conjugation.^[22] For PbS QDs as model system, a near-resonant alignment of VB and tetrathiafulvalenetetracarboxylate HOMO was reasoned from cyclic voltammetry (CV) measurements of the electron oxidation processes.^[23] In general, an effective alignment of QD VB or CB and ligand states is expected to be best achieved with fully conjugated, small molecules with two strongly binding functional groups.^[24] For our study, 2,5-dimercapto-1,3,4-thiadiazole (DMTD) and

2-amino-5-mercapto-1,3,4-thiadiazole (AMTD) served as exemplary symmetric and asymmetric connecting ligands. CV studies report the onset of the oxidation potential of CIS QDs around 0.36 V versus Ag/AgCl, corresponding to a VB level of 5.07 V.^[25] An oxidation potentials of 0.1 V versus Ag/AgCl was reported for DMTD,^[26] suggesting a low energetic offset between VB and HOMO. These values should be considered only as estimate, since the oxidation potentials of the surface bound molecule may differ significantly from values in bulk.

By investigating the ligand-exchanged QD solids with field-effect transistor (FET) and time-resolved optical-pump-terahertz-probe spectroscopy (OTPT) measurements, we show that the alignment of the ligand's HOMO not only leads to an increase of the conductivity by orders of magnitude, but also changes the fundamental transport mechanism. Our work points toward very effective hole transport for the configuration with HOMO-VB alignment.

2. Results and Discussion

CIS QDs were synthesized according to established protocols with oleylamine (OAm) as native stabilizing ligand (CIS-OAm).^[21] The QDs feature significant size and shape variations, as exemplary visualized in the transmission electron microscopy (TEM) micrograph in **Figure 1a**. Straightforward spin-coating of the QD solution allows the deposition of large scale (mm) CIS QD solids as films on arbitrary substrates, where the film thickness can be controlled by the spin-coating conditions. After film deposition, a ligand exchange can be performed by exposing to a ligand solution and washing the abundant ligands. QD solids with the ligands OAm, AMTD, and DMTD were prepared and characterized with UV-vis spectroscopy, IR absorption, scanning electron microscopy (SEM) and small-angle X-ray

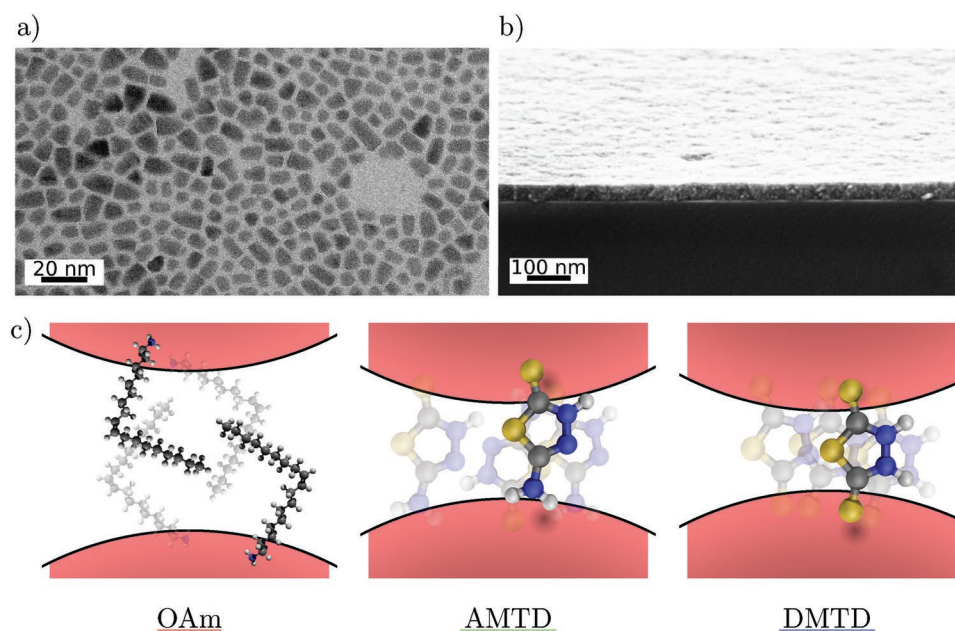


Figure 1. a) TEM image of CIS QDs. The QDs average length is 8 nm, with a diameter of 5 nm. b) SEM image of a CIS QD solid film with DMTD. c) Sketch of the investigated samples. AMTD and DMTD feature two strongly binding endgroups that ensure connecting the QDs. While DMTD binds via two thiones (for tautomeric forms see the Supporting Information) groups, AMTD binds asymmetric via a thion and an amine group to the QDs.

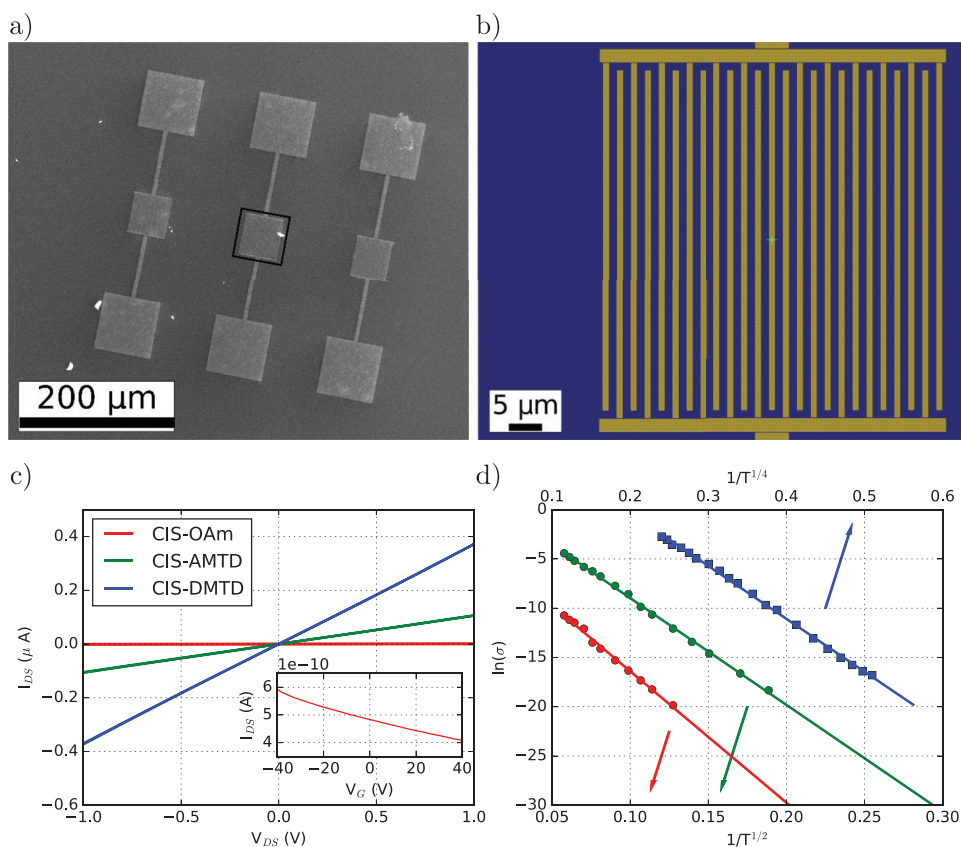


Figure 2. a) SEM image of the device layout for the transport measurements. b) Electrode structure is schematically shown. c) Room-temperature I - V curves and gate-dependent current at a source-drain voltage of 1 V (inset, refer to the Supporting Information for more data). d) Temperature-dependent conductivities of the three samples. CIS-OAm and CIS-AMTD obey a $T^{-1/2}$ conductivity dependence, CIS-DMTD shows a $T^{-1/4}$ behavior.

scattering (SAXS) (see the Supporting Information). Figure 1b displays a SEM image of a cut through an exemplary QD solid film. Homogeneous coverage with uniform thickness can be achieved. The average center-to-center distances within the QD solids were determined by a combination of SAXS and statistical TEM analyses to 6.0 nm for CIS-OAm, 5.9 nm for CIS-AMTD, and 5.4 nm for CIS-DMTD (see the Supporting Information for more details).

The carrier mobilities in the QD solids were investigated in a field-effect transistor geometry (Figure 2a,b).^[27]

The current-voltage behavior at room temperature of the three QD solids is displayed in Figure 2c. The QD solids exhibit a generally linear and point-symmetric I - V behavior at room temperature. The room temperature conductivities σ of the QD solids are $4.7 \times 10^{-5} \text{ S cm}^{-1}$ for CIS-OAm, $8.0 \times 10^{-3} \text{ S cm}^{-1}$ for CIS-AMTD, and $4.3 \times 10^{-2} \text{ S cm}^{-1}$ for CIS-DMTD. The connecting ligand molecules AMTD and DMTD increase the conductivity by two and three orders of magnitude, respectively. These conductivities are still lower than for a bulk CIS crystal ($1.5 \times 10^{-1} \text{ S cm}^{-1}$),^[28] but of the same order of magnitude as polycrystalline films with grain boundaries and a comparable stoichiometric composition $1.6 \times 10^{-2} \text{ S cm}^{-1}$.^[29]

As the hopping distance d influences the hopping probability with $P \propto \exp(-d)$, the reduction of the ligand length as dominant change would reflect exponentially in the measured conductivity.^[10,11,30] However, with the experimental QD separations, no exponential dependence is obtained for the measured

conductivities. Thus, the changed electronic structure within the ligands (HOMO, LUMO of the molecules) must dominate.

In field-dependent transport measurements (Figure 2c), we obtained mobilities of $9.4 \times 10^{-5} \text{ cm V}^{-2} \text{ s}^{-1}$ for the CIS QD solid with CIS-OAm, $1.2 \times 10^{-2} \text{ cm V}^{-2} \text{ s}^{-1}$ for CIS-AMTD, and $2.1 \times 10^{-2} \text{ cm V}^{-2} \text{ s}^{-1}$ for CIS-DMTD. The present CIS QDs exhibit a p-type conductivity, in accordance with the literature on the crystal composition (see the Supporting Information).^[29,31,32] For hopping transport, the temperature dependence of the conductivity can in general be described by

$$\sigma(T) = \sigma_0 \exp \left[- \left(\frac{T_0}{T} \right)^{\nu} \right] \quad (1)$$

with a prefactor σ_0 , the activation energy-dependent characteristic temperature T_0 , and an exponential factor ν which defines the dominant hopping transport mechanism.^[16,33] For uniform interparticle distances and sufficiently high temperatures, the strong distance dependence of the hopping probability results in hopping primarily occurring to adjacent neighboring QDs. This nearest-neighbor hopping (NNH) features an Arrhenius-type behavior with $\nu = 1$. At lower temperatures and in stronger disordered systems, hopping into available states with low activation energies sometimes leads to higher probabilities than the hopping determined by the distance dependence.^[33] The resulting variable-range hopping transport (VRH) depends on the available electronic states and can happen via two processes. Mott-(M-) variable range hopping (M-VRH) is governed by the

density of states (DOS) around the Fermi level E_F and shows a temperature dependence of the conductivity of $\nu = 1/4$ for 3D systems.^[11,34] Efros–Shklovskii hopping (ES-VRH) includes Coulomb interactions that modify the DOS and is especially relevant for doped semiconductors.^[35] This mechanism is, for example, observed at low temperatures, where the Coulomb gap is larger than $k_b T$ and the temperature dependence then follows $\nu = 1/2$.^[16,36] To facilitate distinguishing between the different hopping mechanisms, Zabrodskii and Zinov'eva^[37] introduced an analysis approach employing

$$\ln \left[\frac{d \ln \sigma}{d \ln T} \right] = \ln(\nu T_0^\nu) - \nu \ln(T) \quad (2)$$

The slope of $\ln[d(\ln \sigma)/d(\ln T)]$ versus $\ln T$ allows the extraction of the hopping coefficient ν .^[16,37,38] The data of each sample follows linear trends, which confirms hopping as dominant transport mechanism (see the Supporting Information). Fits to the data result in hopping parameters of $\nu = 0.51$ for the QD solid with CIS-OAm, $\nu = 0.50$ for CIS-AMTD and $\nu = 0.26$ for CIS-DMTD. The choice of the ligand determines the specific VRH processes. The temperature-dependent conductivities are summarized in Figure 2 d: CIS-OAm and CIS-AMTD have a $T^{-1/2}$ temperature dependence of the conductivity. The majority hole carriers in the highly disordered, doped QD solid are strongly influenced by Coulomb interactions and obey the ES-VRH transport mechanism. The DMTD linker seems to provide a constant DOS for the holes that promotes Mott hopping and results in a $T^{-1/4}$ temperature dependence of the conductivity. To understand the differences on a more local scale OPTP spectroscopy was employed.^[39]

While the transport measurements in the FET geometry determine the conductivity as steady-state product of charge carrier concentration n and mobility μ , integrated across the sample, OPTP probes the carriers on a more local scale. OPTP spectroscopy can be used to study the conductivity in a non-contact fashion. The picosecond THz electric field interacts with free charges, changing the electric-field waveform $E(t)$ of the transmitted THz pulse. After optical excitation, the properties of the photogenerated carriers (lifetime, mobility) can be probed by a delayed THz pulse. OPTP provides a frequency-resolved complex conductivity, which is also sensitive to the electronic coupling between the QDs.^[40,41] The experiment is summarized in Figure 3a. The time-resolved experiment allows both the degree of QD coupling and the carrier dynamics (for example, affected by the delocalization of carriers between the QDs) to be addressed simultaneously.

$E(t)$ of the THz probe pulse transmitted through the unexcited sample is shown in Figure 3b. Following optical excitation, the interaction of the THz-electric field with the excited carriers modifies the transmitted THz pulse and the differential change in the THz waveform $\Delta E(t)$ can be recorded. In the CIS QD solids, a damping is accompanied by a phase shift relative to the incident pulse. This is common for carriers in confined systems.^[42] To follow the carrier dynamics, the delay between the optical-pump and the THz probe pulse can be varied. Figure 3c displays a map of ΔE versus t and τ , where the time t is the reference for the THz-electric field (as in Figure 3b) and τ is the delay between optical pump and THz probe.

The frequency (time) integrated ΔE scales with the amount of photogenerated carriers.^[43] It is plotted in Figure 3d for the three samples and two exemplary excitation fluences each. The

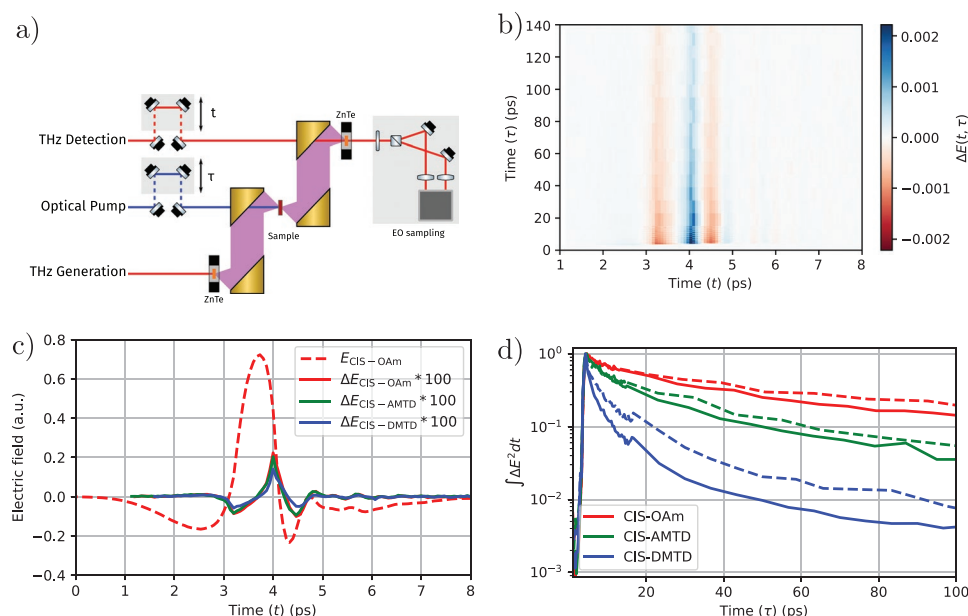


Figure 3. a) Sketch of the OPTP setup. The sample is excited by an optical pulse which arrives prior to the THz pulse, delayed by τ . The THz pulse is generated from an optical pulse in a ZnTe crystal by optical rectification and focused on the sample with off-axis parabolic mirrors. The THz pulse is transmitted through the excited sample and the time-domain t reconstruction of the THz pulse is performed by electro-optical sampling in a ZnTe crystal with a balanced photodiode. b) Experimental ΔE map for CIS-OAm. c) Exemplary ΔE curves at $\tau = 10$ ps together with the THz-electric field transmitted through the unexcited CIS-OAm sample. d) Change of ΔE , time-integrated and normalized with respect to τ for 1.2 μJ (solid lines) and 0.5 μJ (dashed lines) excitation pulse energies.

carrier population of the CIS-OAm QD solid sample excited with a low fluence (0.5 μJ per pulse) shows an almost mono-exponential decay with a lifetime of ≈ 100 ps. Increasing the excitation pulse energy to 1.2 μJ leads to a biexponential decay. Higher fluences generate multiple carriers and multicarrier recombination becomes possible, which annihilates the excess carriers very effectively, leading to a fast initial population decay.^[44] The samples CIS-AMTD and CIS-DMTD show different decay dynamics than CIS-OAm. The decays are much faster and are always biexponential where the short components are more prominent than as for CIS-OAm. As first approximation, this can be understood with the increased carrier mobility: the screening of nonradiative relaxation pathways like defects is increased, but also the probability for multicarrier recombination as the effective amount of accessible carriers for the nonradiative channel is increased.^[45,46] The amount of lifetime shortening has the same systematic than the mobility increases in the FET experiments. In this way, the increased mobility might be disadvantageous for some applications, as the photo-generated carriers are annihilated faster.^[46]

For a more differentiated analysis of the specific transport mechanism, the pump-induced complex photoconductivity can be analyzed. The frequency-dependent complex conductivity for different delay times τ can be extracted using

$$\sigma(\tau, \omega) = -\frac{\epsilon_0 c (1 + n_{\text{Substrate}})}{d} \frac{\Delta T(\tau, \omega)}{T(\tau, \omega)} \quad (3)$$

where ϵ_0 is the vacuum permittivity, c the speed of light, d the thickness of the sample on the substrate, $n_{\text{Substrate}}$ the frequency-dependent complex refractive index of the substrate, T is the Fourier transformation of the THz-electric field transmitted through the unexcited sample, and ΔT is the Fourier transformation of the differential THz-electric field transmitted after photoexcitation (see the Supporting Information for a

tutorial-style, detailed description).^[47] Figure 4 displays the obtained complex conductivities for two representative regimes after photoexcitation.

All samples show a low real zero-bias conductivity for the photogenerated carriers, but a significant imaginary response, which indicates a dominant role of bound or localized carriers. As we observed no band-like transport in the previous experiments, this is expected: in comparison to band transport, hopping events from particle to particle are rare, thus the overall response of the material is less likely to be Drude-like. For CIS-OAm and CIS-AMTD, the real part of σ becomes negative after photoexcitation. This is a rare observation. Normally, the photoexcitation enhances the conductivity as the concentration of mobile carriers is increased. Negative photoconductivities have been reported earlier for photoexcitation of doped materials. When the interaction of the photogenerated carriers with, for example, intrinsic majority carriers leads to a reduction of the mobility while the relative carrier concentration is almost constant (because of high intrinsic concentrations), a negative differential conductivity can be obtained. For example, in graphene, a negative photoconductivity was observed via OPTP spectroscopy.^[48,49] In the doped high-mobility samples, electron heating increases the carrier scattering rate, without increasing the effective carrier concentration significantly. A net decrease of the photoconductivity was also reported for CdSe nanorods with an electron acceptor molecule. In time-resolved OPTP experiments, after a picosecond trapping of the electrons, the delocalized hole interacts with the Coulomb potential of the reduced electron acceptor. This leads to an effective reduction of the hole mobility in the nanorods.^[50] In doped Si nanowires, carriers trapped at dopant ions act as Coulomb scatterers, reducing the mobility.^[51] A similar observation was made for p-type $\text{Pb}_{1-x}\text{Sn}_x\text{Te}$ films.^[52]

The remarkable aspect in case of the CIS QD solids is the dependence of the photoinduced conductivity on the connecting

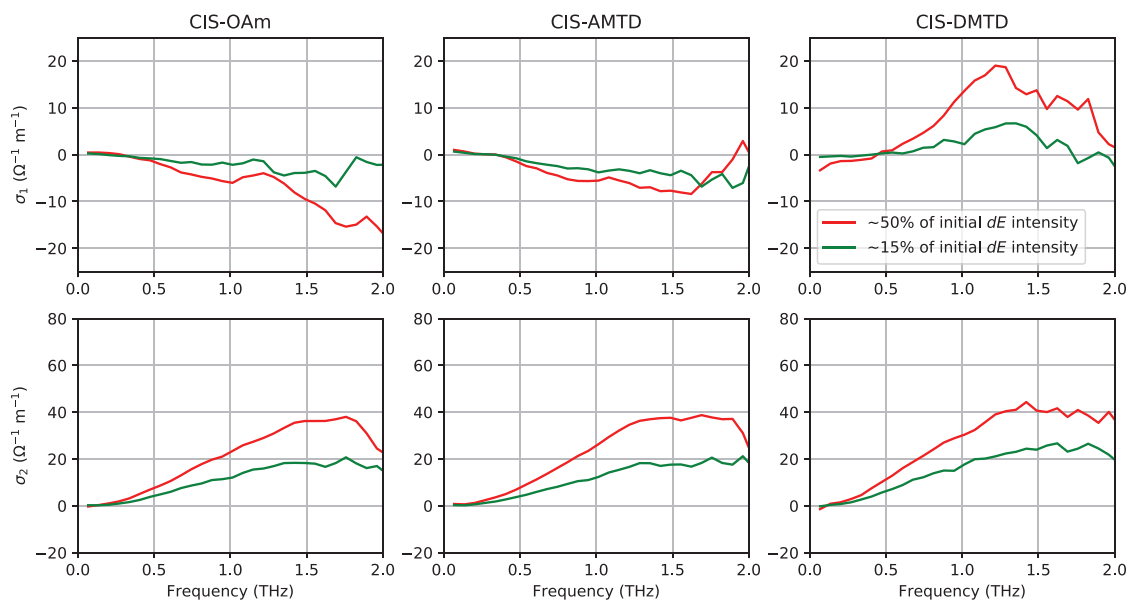


Figure 4. Frequency-dependent photoconductivities $\sigma(\omega) = \sigma_1(\omega) + i\sigma_2(\omega)$ obtained for excitation with 1.2 μJ pulse energy at 650 nm. Displayed are data at two representative τ after the fast initial dynamics (compare Figure 3d). The upper panel shows the real part, the lower the imaginary part of the complex conductivity as obtained with Equation (3).

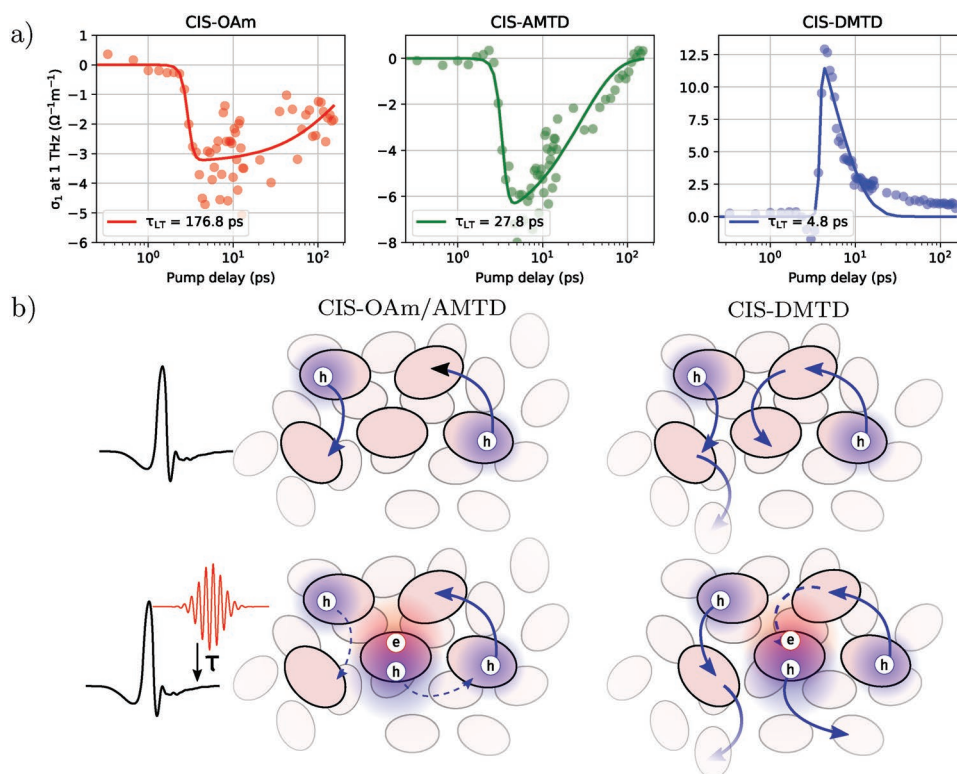


Figure 5. a) Time-dependence of the real part of the conductivity σ_1 at the frequency around the maximum value (1 THz). The data (dots) have been fitted with monoexponential decays (solid line). While for CIS-OAm and CIS-AMTD, this can roughly capture the time evolution, for CIS-DMTD the decay is clearly biexponential, as the carrier dynamics. b) Sketch of the proposed effect. Without optical excitation, the movement of the intrinsic carriers (holes) is probed by the THz pulse. Because of efficient M-VRH, holes in CIS-DMTD have a much higher mobility than in CIS-OAm and CIS-AMTD, where the transport is influenced by Coulomb interaction (ES-VRH). Optical excitation generates electron–hole pairs. Trapping leads to localized charges that act on the intrinsic holes by Coulomb interaction. The relative change is more drastic for CIS-OAm and CIS-AMTD than for CIS-DMTD. There, the transport is less influenced by Coulomb interaction and the conductivity gain by the carrier concentration increase outweighs a potential small mobility decrease.

ligands. The ligand exchange is not expected to significantly change the QD's internal structure. In that case, one would also expect stronger changes from CIS-OAm to CIS-AMTD and CIS-DMTD than from CIS-OAm and CIS-AMTD to CIS-DMTD (as observed). Thus, we assume the change from negative to positive conductivity to mostly originate from the general change in the transport process. For another view, the time evolution of the conductivity peaks are plotted in Figure 5a.

The general behavior of CIS-OAm and CIS-AMTD is very similar: a minimum conductivity is reached after ≈ 5 ps and then recovers on timescales of the carrier relaxation time. For CIS-DMTD, the maximum conductivity is reached directly after photoexcitation and also recovers during the carrier lifetime. This difference can be reasoned within the picture obtained from the temperature-dependent studies, schematically displayed in Figure 5b. In CIS QD solids, majority carriers are holes that lead to a significant dark current in all three samples. Photoexcitation generates electron–hole pairs, increasing the carrier concentration. The photogenerated carriers interact with the intrinsic holes via Coulomb interaction. For CIS-OAm and CIS-AMTD Coulomb interactions dominate the hopping probability and the additional carriers increase the hopping activation energy, lowering the carrier mobility. Regarding the amount of intrinsic holes, the net carrier concentration increase is small compared to the decrease in mobility, resulting in the conductivity decrease. This was also observed for other trapped

carriers in semiconductor nanostructures, where Coulomb interactions can lead to a carrier localization and reduction of the mobility.^[50,51,53,54] For CIS-DMTD, an alignment of the QD VB and the molecules HOMO provides states for an efficient M-VRH transport, leading to a significantly increased mobility of the majority carriers (holes). Under such conditions, the DOS is not significantly altered by additional carriers, so that the hopping probability for M-VRH is almost constant. Changes are but negligible compared to the high intrinsic (dark) mobility. Then, every photogenerated hole leads to an increase in conductivity and the carrier recombination results in a relaxation of this increase, as observed in the experiments. This demonstrates that the type of the hopping mechanisms not only determines the hopping probability (and conductivity), but also alters the system's response to photoexcitation. As the exact mechanism depends on the employed ligands, the strategy of using the ligand's electronic structure to influence the transport is very flexible.

3. Conclusions

In conclusion, we explored the concept of influencing charge carrier transport through QD solids by the electronic structure of the connecting ligand molecules. By replacing the intrinsic ligands which stabilize the particles with two exemplary short

bivalent linkers, we were able to increase the hopping mobilities and conductivities by several orders of magnitude, which is not due to a distance decrease. Temperature-dependent conductivity studies show distinct differences in the general transport mechanisms from Coulomb interaction-governed ES- to DOS-determined M-VRH between the CIS-OAm and CIS-AMTD QD solids and CIS-DMTD. OPTP experiments show a negative photoconductivity for CIS-OAm and CIS-AMTD, but a positive photoconductivity for CIS-DMTD. This observation can be explained by a picture employing carrier trapping and a decrease of the hopping probability for Efros–Shklovskii hopping by the Coulomb interactions with the intrinsic holes. The effect is less drastic for Mott hopping. In CIS-DMTD, the ligand provides states for efficient Mott hopping, resulting in a high intrinsic hole mobility and potential relative reductions are negligible compared to the carrier concentration increase, leading to a conductivity increase. In future studies, this mechanism needs further investigation of the nature of the Coulomb interactions between intrinsic and photogenerated carriers and the influence on transport mechanism, with special regards to the electronic structure of the ligands. For example, employing OPTP using a gated sample could address those questions, since the amount of intrinsic carriers could be tuned.

4. Experimental Section

CIS QD Synthesis and QD Solid Preparation: CIS QDs were synthesized based on a modified protocol of Panthani et al.^[21] 0.50 mmol copper(I) acetate (61 mg), 0.50 mmol indium(III) chloride (0.11 g), and 1.0 mmol selenourea (0.12 g) were mixed in a 25 mL three-neck flask and connected to a Schlenk line afterward. 10 mL (*Z*)-octadec-9-en-1-amine (oleylamine) was then added to the solution and the dispersion was kept stirring at 5.0×10^{-2} mbar and 60°C for 60 min. After another 60 min under nitrogen atmosphere at 110 °C, the reaction solution was heated to 240°C for 60 min. Then, the solution was cooled to room temperature. Before purification, the dispersion was mixed with 3 mL of trioctylphosphine and 1 mL of toluene to achieve an improved colloidal stability. 2 mL 2-propanol was added and the solution was centrifuged at $2105 \times g$ for 5 min to remove ill-stabilized particles. For the precipitation, 20 mL 2-propanol was added to the colored supernatant which was subsequently centrifuged for 15 min at $2105 \times g$. The slightly colored supernatant with smaller particles was removed and the residual QDs were dissolved in 4 mL toluene. This colloidal solution was mixed with 15 mL 2-propanol and centrifuged again at $2105 \times g$ for 15 min. The colorless supernatant was again discarded and the residual particles were dissolved in 8 mL *n*-hexane.

Charge Transport Measurements: Device Fabrication and Setup: Electrode patterns consisting of 25 interdigitated fingers (24 channels) with a gap length of 1 μm each and a width of 50 μm were prepared by electron beam lithography with a subsequent deposition of thermal evaporated titanium (3 nm), followed by gold (27 nm). In order to achieve a field-effect transistor geometry with both top electrodes, highly doped silicon (back gate) with a thermally grown oxide layer of 300 nm (dielectric) was utilized as substrate. The transport measurements were performed in a probe station under vacuum from Lake Shore Cryotronics (VF4TP4) and with the use of a Keithley 2400-SCS.

Charge Transport Measurements: Sample Preparation: The substrates with the predeposited gold electrodes were cleaned for 2 min under air plasma to remove contaminants from the surface and subsequently transferred into a nitrogen filled glove box. 30 μL of CIS solution in *n*-hexane was given on the substrate (1 cm, volume depended on the

surface area) and let spread over the substrate for 3 s. Subsequently the spincoater was switched on for 15 s at 2000 rpm. In order to establish a nanocrystal film thickness of 25 nm, this procedure was repeated 2 times (3 in total). Afterward, 60 μL of a linker solution (2 mmol L⁻¹ in acetonitrile) was carefully applied to the film and slowly let dry within 10 min. This step was repeated once (2 in total) for a complete ligand exchange. The fully dried films were first washed with acetonitrile to remove any abundant linker by applying 0.5 μL solvent to the film, waiting 5 s and switching the spin-coater on (2000 rpm, 15 s). This step was again repeated 3 times (4 in total, 200 μL) afterward also repeated with *n*-hexane in the same way to remove not interlinked CIS particles and abundant oleylamine. The whole process ensured a complete ligand exchanged layer and is once repeated to gain the used 50 nm thick nanocrystal film (Figure 1b).

OPTP Spectroscopy: Sample Preparation: 60 mL of the as-synthesized CIS QD solution in *n*-hexane was given into a cavity (0.5 mm deep, 10 mm diameter) of a polytetrafluoroethylene (PTFE) substrate under nitrogen atmosphere. After drying, the whole substrate was put into a ligand solution (screw top jar, 2.0 mmol L⁻¹ DMTD or AMTD in acetonitrile). In case of the CIS-native samples, the substrate was just put into pure acetonitrile. After 12 h, the substrates were carefully rinsed with acetonitrile for 1 min to remove redundant ligand molecules. That process yielded in a film thickness of 1 μm.

OPTP Spectroscopy: Measurements: The prepared QD solid films were mounted in the self-build OPTP setup. Optical excitation was performed with 480, 500, 650, 850, and 1220 nm and 0.5 and 1.2 mW, respectively. The terahertz radiation was generated using optical rectification in a ZnTe crystal, the electric field was measured after passing through the sample by the electro-optical effect. All measurements were performed under a nitrogen atmosphere. Comparing the electric field $E(t)$ after passing through the sample for different times τ after the excitation of the sample with the electric field after passing through the unexcited sample, the optically induced change of the electric field $dE(t, \tau)$ was obtained.

Supporting Information

Supporting Information is available from the Wiley Online Library or from the author.

Acknowledgements

This work was supported by the Clusters of Excellence “Advanced Imaging of Matter” and “The Hamburg Centre for Ultrafast Imaging” of the Deutsche Forschungsgemeinschaft (DFG) (EXC 2056 – project ID 390715994 and EXC 1074 – project ID 194651731). The authors thank Tobias Kampfrath (FHI Berlin) and Carmen Herrmann (University of Hamburg) for fruitful discussions.

Conflict of Interest

The authors declare no conflict of interest.

Keywords

hopping transport, ligand exchange, photoc conductivity, quantum dot solids, THz spectroscopy

Received: June 25, 2019

Revised: October 14, 2019

Published online: November 18, 2019

- [1] L. E. Brus, *J. Chem. Phys.* **1984**, *80*, 4403.
- [2] M. A. Boles, D. Ling, T. Hyeon, D. V. Talapin, *Nat. Mater.* **2016**, *15*, 141.
- [3] C. R. Kagan, E. Lifshitz, E. H. Sargent, D. V. Talapin, *Science* **2016**, *353*, aac5523.
- [4] Y. Shirasaki, G. J. Supran, M. G. Bawendi, V. Bulović, *Nat. Photonics* **2013**, *7*, 13.
- [5] A. R. Uhl, A. Rajagopal, J. A. Clark, A. Murray, T. Feurer, S. Buecheler, A. K.-Y. Jen, H. W. Hillhouse, *Adv. Energy Mater.* **2018**, *8*, 1801254.
- [6] G. H. Carey, A. L. Abdelhady, Z. Ning, S. M. Thon, O. M. Bakr, E. H. Sargent, *Chem. Rev.* **2015**, *115*, 12732.
- [7] P. Guyot-Sionnest, *J. Phys. Chem. Lett.* **2012**, *3*, 1169.
- [8] K. Whitham, J. Yang, B. H. Savitzky, L. F. Kourkoutis, F. Wise, T. Hanrath, *Nat. Mater.* **2016**, *15*, 557.
- [9] E. Talgorn, Y. Gao, M. Aerts, L. T. Kunneman, J. M. Schins, T. J. Savenije, M. A. van Huis, H. S. J. van der Zant, A. J. Houtepen, L. D. A. Siebbeles, *Nat. Nanotechnol.* **2011**, *6*, 733.
- [10] Y. Liu, M. Gibbs, J. Puthussery, S. Gaik, R. Ihly, H. W. Hillhouse, M. Law, *Nano Lett.* **2010**, *10*, 1960.
- [11] D. Yu, C. Wang, B. L. Wehrenberg, P. Guyot-Sionnest, *Phys. Rev. Lett.* **2004**, *92*, 216802.
- [12] A. T. Fafarman, W.-k. Koh, B. T. Diroll, D. K. Kim, D.-K. Ko, S. J. Oh, X. Ye, V. Doan-Nguyen, M. R. Crump, D. C. Reifsnyder, C. B. Murray, C. R. Kagan, *J. Am. Chem. Soc.* **2011**, *133*, 15753.
- [13] J. Lauth, J. Marbach, A. Meyer, S. Dogan, C. Klinke, A. Kornowski, H. Weller, *Adv. Funct. Mater.* **2014**, *24*, 1081.
- [14] G. H. Carey, L. Levina, R. Comin, O. Voznyy, E. H. Sargent, *Adv. Mater.* **2015**, *27*, 3325.
- [15] N. Ray, N. E. Staley, D. D. W. Grinolds, M. G. Bawendi, M. A. Kastner, *Nano Lett.* **2015**, *15*, 4401.
- [16] H. Liu, A. Pourret, P. Guyot-Sionnest, *ACS Nano* **2010**, *4*, 5211.
- [17] M. S. Azzaro, A. Dodin, D. Y. Zhang, A. P. Willard, S. T. Roberts, *Nano Lett.* **2018**, *18*, 3259.
- [18] A. André, M. Weber, K. M. Wurst, S. Maiti, F. Schreiber, M. Scheele, *ACS Appl. Mater. Interfaces* **2018**, *10*, 24708.
- [19] J. Liu, X. Huang, F. Wang, W. Hong, *Acc. Chem. Res.* **2019**, *52*, 151.
- [20] G. Xu, S. Zeng, B. Zhang, M. T. Swihart, K.-T. Yong, P. N. Prasad, *Chem. Rev.* **2016**, *116*, 12234.
- [21] M. G. Panthani, V. Akhavan, B. Goodfellow, J. P. Schmidtke, L. Dunn, A. Dodabalapur, P. F. Barbara, B. A. Korgel, *J. Am. Chem. Soc.* **2008**, *130*, 16770.
- [22] M. B. Teunis, M. Nagaraju, P. Dutta, J. Pu, B. B. Muhoberac, R. Sardar, M. Agarwal, *Nanoscale* **2017**, *9*, 14127.
- [23] M. Scheele, D. Hanifi, D. Zherebetsky, S. T. Chourou, S. Axnanda, B. J. Rancatore, K. Thorkelsson, T. Xu, Z. Liu, L.-W. Wang, Y. Liu, A. P. Alivisatos, *ACS Nano* **2014**, *8*, 2532.
- [24] R. D. Harris, S. Bettis Homan, M. Kodaimati, C. He, A. B. Nepomnyashchii, N. K. Swenson, S. Lian, R. Calzada, E. A. Weiss, *Chem. Rev.* **2016**, *116*, 12865.
- [25] Y. Yang, H. Zhong, Z. Bai, B. Zou, Y. Li, G. D. Scholes, *J. Phys. Chem. C* **2012**, *116*, 7280.
- [26] E. Shouji, Y. Yokoyama, J. M. Pope, N. Oyama, D. A. Buttry, *J. Phys. Chem. B* **1997**, *101*, 2861.
- [27] C. R. Kagan, C. B. Murray, *Nat. Nanotechnol.* **2015**, *10*, 1013.
- [28] H. T. Shaban, M. Mobarak, M. M. Nassary, *Phys. B* **2007**, *389*, 351.
- [29] S. M. Firoz Hasan, M. A. Subhan, K. M. Mannan, *Opt. Mater.* **2000**, *14*, 329.
- [30] U. Simon, *Adv. Mater.* **1998**, *10*, 1487.
- [31] S. B. Zhang, S.-H. Wei, A. Zunger, H. Katayama-Yoshida, *Phys. Rev. B* **1998**, *57*, 9642.
- [32] S. Draguta, H. McDaniel, V. I. Klimov, *Adv. Mater.* **2015**, *27*, 1701.
- [33] M. S. Kang, A. Sahu, D. J. Norris, C. D. Frisbie, *Nano Lett.* **2011**, *11*, 3887.
- [34] N. F. Mott, *Philos. Mag.* **1969**, *19*, 835.
- [35] A. L. Efros, B. I. Shklovskii, *J. Phys. C: Solid State Phys.* **1975**, *8*, L49.
- [36] P. Guyot-Sionnest, *J. Phys. Chem. Lett.* **2012**, *3*, 1169.
- [37] A. G. Zabrodski, K. N. Zinov'eva, *Sov. Phys. JETP* **1984**, *59*, 425.
- [38] A. Yildiz, Ş. Horzum, N. Serin, T. Serin, *Appl. Surf. Sci.* **2014**, *318*, 105.
- [39] M.-J. Sher, J. A. Bartelt, T. M. Burke, A. Salleo, M. D. McGehee, A. M. Lindenberg, *Adv. Electron. Mater.* **2016**, *2*, 1500351.
- [40] R. Ulbricht, E. Hendry, J. Shan, T. F. Heinz, M. Bonn, *Rev. Mod. Phys.* **2011**, *83*, 543.
- [41] P. Kužel, H. Němec, *Adv. Opt. Mater.* **2019**, 1900623, <https://doi.org/10.1002/adom.201900623>.
- [42] F. Wang, J. Shan, M. A. Islam, I. P. Herman, M. Bonn, T. F. Heinz, *Nat. Mater.* **2006**, *5*, 861.
- [43] J. Lloyd-Hughes, T.-I. Jeon, *J. Infrared, Millimeter, Terahertz Waves* **2012**, *33*, 871.
- [44] V. I. Klimov, A. A. Mikhailovsky, D. W. McBranch, C. A. Leatherdale, M. G. Bawendi, *Science* **2000**, *287*, 1011.
- [45] Y. Gao, C. S. S. Sandeep, J. M. Schins, A. J. Houtepen, L. D. A. Siebbeles, *Nat. Commun.* **2013**, *4*, 2329.
- [46] M. Rafipoor, R. Koll, J.-P. Merkl, L. S. Fruhner, H. Weller, H. Lange, *Small* **2019**, *15*, 1803798.
- [47] H. J. Joyce, J. L. Boland, C. L. Davies, S. A. Baig, M. B. Johnston, *Semicond. Sci. Technol.* **2016**, *31*, 103003.
- [48] J. Lu, H. Liu, J. Sun, *Nanotechnology* **2017**, *28*, 464001.
- [49] G. Jnawali, Y. Rao, H. Yan, T. F. Heinz, *Nano Lett.* **2013**, *13*, 524.
- [50] Y. Yang, K. Wu, A. Shabaev, A. L. Efros, T. Lian, M. C. Beard, *ACS Energy Lett.* **2016**, *1*, 76.
- [51] E. Baek, T. Rim, J. Schütt, C.-k. Baek, K. Kim, L. Baraban, G. Cuniberti, *Nano Lett.* **2017**, *17*, 6727.
- [52] M. a. B. Tavares, M. J. da Silva, M. L. Peres, S. de Castro, D. a. W. Soares, A. K. Okazaki, C. I. Fornari, P. H. O. Rappl, E. Abramof, *Appl. Phys. Lett.* **2017**, *110*, 042102.
- [53] C. H. Lui, A. J. Frenzel, D. V. Pilon, Y.-H. Lee, X. Ling, G. M. Akselrod, J. Kong, N. Gedik, *Phys. Rev. Lett.* **2014**, *113*, 166801.
- [54] Y. Han, M. Fu, Z. Tang, X. Zheng, X. Ji, X. Wang, W. Lin, T. Yang, Q. Chen, *ACS Appl. Mater. Interfaces* **2017**, *9*, 2867.